Electrochimica Acta 361 (2020) 137040

Contents lists available at ScienceDirect

Electrochimica Acta

journal homepage: www.elsevier.com/locate/electacta

Research Paper

Ni/NiO nanosheets for alkaline hydrogen evolution reaction: In situ electrochemical-Raman study

Alaa Y. Faid[a,*], Alejandro Oyarce Barnett[b,c], Frode Seland[a], Svein Sunde[a]

[a] Department of Materials Science and Engineering, Norwegian University of Science and Technology, Trondheim, Norway
[b] SINTEF Industry, New Energy Solutions Department, Trondheim, Norway
[c] Department of Energy and Process Engineering, Norwegian University of Science and Technology

ARTICLE INFO

Article history:
Received 30 July 2020
Accepted 30 August 2020
Available online 3 September 2020

Keywords:
Ni/NiO
Hydrogen evolution
In situ raman
Alkaline electrolysis

ABSTRACT

Nickel/Nickel oxide (Ni/NiO) nanosheets heterostructure is a cheap and active catalyst for hydrogen evolution reaction (HER) in alkaline electrolytes. However, the reason for this activity is still under debate. Herein in-situ Raman electrochemistry has been established as a method to probe interfacial intermediates and correlate the performance of various nickel catalysts (Ni, NiO, and Ni/NiO nanosheets) during HER. In-situ Raman spectroscopy demonstrated that Ni/NiO nanosheet heterostructure maintained β-Ni(OH)$_2$ species initially, which may contribute to the superior initial HER activity. Ni/NiO nanosheets lost β-Ni(OH)$_2$ species by preserving a high cathodic overpotential (-0.4 V vs. RHE) for 2000 sec. The results confirmed the importance of Ni metal sites in addition to NiO sites and maintaining hydroxide species for superior and durable HER activity. These results can be utilized to design an efficient and durable catalyst for alkaline electrolyzers for the sustainable production of hydrogen.

1. Introduction

Hydrogen represents a clean alternative energy carrier that may provide a means of storing and distributing energy from renewables and mitigate the consequences of increased global energy demands [1]. Water electrolysis is a good choice to produce hydrogen from renewable sources [1]. Anion exchange membrane water electrolysis (AEMWE) has acquired substantial attention, offering a combination of high efficiency and low-cost catalysts, membranes, and construction materials [2,3].

From an activity and cost perspective, transition metal/metal oxide (M/MO) heterostructures, such as Ni/NiO, are particularly interesting, due to their low cost and high activity for hydrogen evolution reaction (HER) in alkaline electrolytes [4]. A synergistic, electronic interaction between the metal and the oxide has been proposed as the reason for the enhanced HER performance. Strmcnik et al. inferred that the dissociation of H_2O is an essential step for HER in alkaline conditions and that M/MO plays a reactive role in water dissociation [5]. Ni/NiO catalysts can be the key for designing active and cheap catalyst at which H adsorption is favored at metallic Ni^0 and NiO has a high affinity for the formation of adsorbed hydroxyl species, OH_{ads} [5]. Wang Yong's team found that the Ni^0 at the Ni/NiO interface is critical for high catalytic activity [6]. However, Dong et al. found that slightly oxidized Ni atoms, not Ni^0 atoms, are responsible for the superior HER performance at the Ni/NiO interface [7]. Oshchepkov et al. found ten times enhancement of the activity of Ni due to the presence of NiO on the metallic Ni surface [8]. Gong et al. showed that Ni/NiO core-shell heterostructures offer an HER activity similar to that of Pt, but deteriorates after 24 hrs [9]. Danilovic et al. showed that Ni(OH)$_2$/Ni has an activity improvement by a factor of four compared to Ni(OH)$_2$-free Ni surfaces [10]. Bates et al. found that the synergistic HER enhancement of Ni/NiO is due to NiO content and Cr_2O_3 appears to stabilize NiO under HER conditions [11]. As we can see from the literature above, Ni/NiO or Ni/Ni(OH)$_2$ is a cheap and active catalyst for hydrogen evolution reaction (HER) in alkaline electrolytes. However, the reason for this activity is still under debate and more in-situ investigations are needed to reveal the reasons for the activity enhancements.

Raman spectroscopy is an essential tool for in-situ investigations of electrocatalytic reactions as it provides precise information about reaction intermediates and polarization induced vibrations [12]. A change in polarizability during molecular vibration is required to observe the Raman spectra of samples. The metals with a single atom primitive unit cell do not display any polarizability change, and hence no Raman spectrum is obtained [13]. In-situ Ra-

* Corresponding author. Alaa Y. Faid. Norwegian University of Science and Technology, Department of Materials Science and Engineering, Trondheim, Norway.
E-mail address: alaa.faid@ntnu.no (A.Y. Faid).

https://doi.org/10.1016/j.electacta.2020.137040

man measurements are needed to investigate intermediate formation during HER for Ni/NiO and changes of nickel oxidation states.

In this work, we aim to investigate the role of the nickel catalyst oxidation state (Ni, NiO, and Ni/NiO) on HER activity and monitoring its stability under HER conditions via in situ Raman spectroscopy. As we will demonstrate below Ni/NiO nanosheets have an exceptional HER activity compared to bare Ni or NiO. In-situ Raman measurements reveal that surface β-Ni(OH)$_2$ initially present at Ni/NiO nanosheets is preserved during the HER to much lower potentials than at Ni or NiO nanosheets. We will argue below that this explains the superior HER activity of Ni/NiO. However, β-Ni(OH)$_2$ is eventually reduced at very negative potential (−0.4 V vs. RHE for 2000 sec).

2. Experimental

2.1. Catalyst synthesis

10 mmol of nickel nitrate hexahydrate Ni(NO$_3$)$_2$.6H$_2$O (≥97.0%, Sigma Aldrich) was dissolved in 500 ml deionized water (18.2 MΩ cm, 3 ppb TOC, Milli-Q water). The solution mixture was stirred at 750 rpm for 15 min. 200 ml of 0.15 M NaBH$_4$ (98%, Sigma Aldrich) was added dropwise to the precursor solution. Bubbles were observed during NaBH$_4$ addition. To ensure complete reduction, the solution mixture was stirred for another 1 hour. The precipitate was centrifuged for 6 times at 8000 rpm for 6 min and cleaned with water and ethanol for 3 times.

The produced precipitate was dried under vacuum at 60 °C overnight. Various oxidation states of nickel were attained by annealing the produced catalyst in multiple atmospheres. For NiO, the dried powder was annealed in the air for 6 hrs at 500 °C. For Ni, the dried powder was annealed in 5%H$_2$/Ar at 500 °C for 6 hrs. For Ni/NiO, NiO powder was annealed in 5% H$_2$/Ar at 500 °C for 6 hrs with a ramping rate of 10 °C/min.

2.2. Structural and electrochemical characterization

The morphology and structure of produced catalysts were studied using scanning electron microscopy Hitachi S-5500 FESEM. Structural and crystalline characteristics were investigated using a Bruker D8 A25 DaVinci X-ray device equipped with Cu$_{K\alpha}$ radiation with 1.5425 Å wavelength. Diffraction patterns were acquired between 2θ values of 15 and 75 using a step size of 0.3 [2θ]. Ex-situ Raman spectroscopy was carried out using the WITec alpha300 R Confocal Raman device equipped with a 532 nm laser. Raman spectrum was obtained after 10 accumulations for 10 sec from 100 to 1250 cm^{-1}.

Surface electronic states and composition were carried out by X-ray photoelectron spectroscopy (XPS). The XPS spectra were collected within an Axis Ultra DLD instrument (Kratos Analytical) equipped with a monochromatic Al X-ray source. The specific surface area of catalyst powder was determined using the N$_2$ adsorption-desorption Brunauer-Emmett-Teller method (BET) measured by a TRISTAR 3000 device for surface area and porosity analyzer. The dried samples were degassed at 250 °C under vacuum overnight before the measurement.

2.3. Electrochemical measurements

The electrochemical characterization was conducted in a three-electrode cell using a rotating disk electrode (PINE Research Instrumentation) with a multichannel (Ivium-n-Stat) potentiostat workstation. Carbon paper (Toray 090) was served as the counter-electrode. Hg/HgO (Pine Research) was used as the reference electrode. Working electrodes were fabricated by depositing the catalyst on glassy carbon (GC) electrodes (5 mm diameter, Pine Research).

The GC electrodes were polished using aqueous alumina Al$_2$O$_3$ suspension (5 and 0.25 μm, Allied High-Tech Products, Inc.) on polishing pads. The GC electrode then sonicated in 1 M KOH for 5 min to dissolve any embedded alumina and then rinsed with water and dried in air. To prepare catalyst ink, 10 mg of catalyst was dispersed in 1.0 mL of a solution containing [water, isopropanol, and 5 wt% Nafion solution (1:1:0.01)]. The ink was sonicated for 30 min in an ice bath. The ink was pipetted into a pretreated GC surface to give a loading of 250 μg/cm^2 and dried under an ambient environment.

The electrochemical measurements were conducted in the N$_2$-saturated 1 M KOH electrolyte at room temperature (20 ± 2 °C). The electrolyte was prepared by using KOH (≥85% KOH basis, Sigma Aldrich) and water (18.2 MΩ.cm, Milli-Q water). The electrolyte was purified according to the procedure reported by Trotochaud et.al [14]. The electrolyte was purged for 30 min with N$_2$ gas before usage and during the experiment to remove any dissolved gases during electrochemical measurements.

Before the measurement of linear sweep voltammetry (LSV), the working electrode underwent electrochemical activation by cycling between −0.8 to −1.5 V vs Hg/HgO at a scan rate of 100 mV/sfor 50 cycles until getting reproducible cyclic voltammogram (CV). The LSV polarization curves were recorded in a potential range of-0.8 to −1.5 V vs Hg/HgO at a sweep rate of 1 mV/s at 1600 rpm. The ohmic (IR) drop was compensated at 85% of the ohmic resistance measured by electrochemical impedance spectroscopy (EIS) technique at −1.3 V versus Hg/HgO. The EIS test was collected in a frequency range of 0.1 − 10^5 Hz with an amplitude of 10 mV alternative current (AC) perturbation. The electrochemical data presented is the reproducible data of three inks for the same catalyst powder.

The ECSA was measured by the electrochemical double-layer capacitance method. The CV used for electrochemical double-layer capacitance (C$_{dl}$) calculation was acquired in a potential window where no faradaic process occurred from 0.975 to 1.175 V vs Hg/HgO at 50, 100, 150, 200, and 250 mV/s. To derive the C$_{dl}$, the following equation was used:

$$C_{dl}=\frac{Ic}{\nu} \quad (1)$$

where C$_{dl}$ is the double-layer capacitance of the electroactive materials, Ic is charging current, and ν is the scan rate. The ECSA of a catalyst sample was calculated from the double-layer capacitance according to the following equation:

$$ESCA=\frac{C_{dl}}{C_s} \quad (2)$$

where C$_s$ is the specific capacitance (0.040 mF/cm^2) [15]

Short-term durability was measured using chronoamperometric responses at a fixed overpotential of −0.4 V vs RHE for 10,000 sec.

The potential was corrected using the following equation:

$$E_{compensated} = E_{measured} - iR \quad (3)$$

where $E_{compensated}$ and $E_{measured}$ denote as the compensated and measured potentials, respectively [2]

All measured potentials were converted to a reversible hydrogen electrode (RHE) using the following equation: [1]

$$E_{vs.RHE} = E_{vs.Hg/HgO} + 0.098 + 0.059pH \quad (4)$$

2.4. In-situ raman measurements

In-situ Raman measurements were performed with a home-made Teflon cell with a quartz window. The catalyst deposited on GC (pine research), a carbon paper (fuel cell store), and Hg/HgO

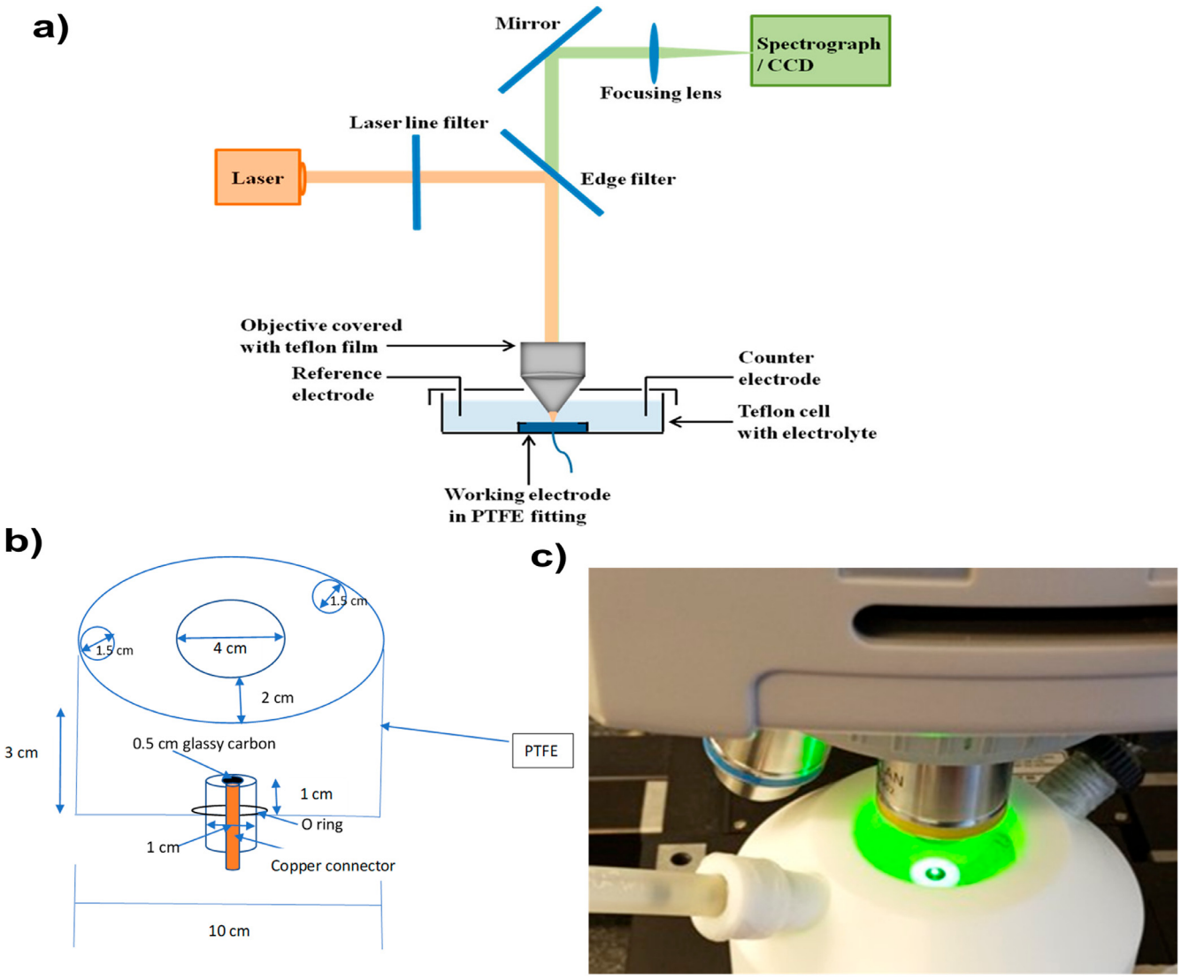

Fig. 1. a) Schematics of in-situ (electrochemical) Raman spectroscopy, [22] b) cell design, and c) image of the in-situ Raman electrochemical cell used in this work. .

(pine research) was used as a working, counter, and reference electrode, respectively as in Fig. 1. In-situ Raman spectra were recorded using a WITec alpha300 R Confocal Raman microscope equipped with a 532 nm laser with a power of 5.0 mW. The Raman device is coupled with Zeiss EC Epiplan 10x objective and G1: 600 g/mm BLZ= 500 nm grating.

Before each experiment, the surface of the glassy carbon electrode was mechanically polished with μm-sized alumina powders, then sonicated in 1 M KOH for 5 min to dissolve any embedded alumina and then rinsed with water and dried in air. For the Raman experiments, purified N_2-saturated 1 M KOH electrolyte was prepared. An optically transparent quartz glass window through which the laser is emitted on the working electrode used to protect the solution or electrode from being contaminated and interfered by the ambient atmosphere. All the experiments were conducted at room temperature (20 $\pm$ 2 °C). All the data points were processed using origin Software. The insitu Raman data presented is the reproducible data of three inks used for the same catalyst powder.

To stabilize the catalyst surface, the working electrode is subject to 10 CVs from −0.1 V to 0.48 V vs RHE at 100 mV/s and the stable CV is shown in the main manuscript. We restricted ourselves below 0.5 Vvs RHE to avoid contributions from electrochemically formed β-Ni(OH)$_2$ [16,17,18]. In situ Raman measurements were done at constant positive and negative potentials (−0.2, −0.1, 0, 0.1, and 0.2 V vs RHE) were applied using an (Ivium-n-Stat) potentiostat for 600 sec. In situ chronoamperometry study was done at -0.4 V vs. RHE for 10,000 sec from 100 to 2000 cm^{-1}. In situ Raman spectra after 10,000 sec were collected in 100 to 3800 cm^{-1} range. The Raman spectra were collected at the applied potentials in 1 M KOH every 10 accumulations (10 sec/accumulation). The ex-situ Raman spectra of catalysts after HER was carried out after removing electrode from the Raman cell and electrode exposed to an ambient atmosphere. The spectrum shifts were calibrated using a silicon wafer Raman peak at 520.7 cm^{-1}.

3. Results

3.1. Structural characterization

Fig. 2a and 1b show SEM images of nickel catalyst synthesized by nickel (II) precursors by sodium borohydride described in the supplementary information. The produced nickel catalysts (Ni, NiO, and Ni/NiO) showed an irregular morphology that appears to consist of curved sheets. The SEM images show that nanosheets are composed of an interconnected net-

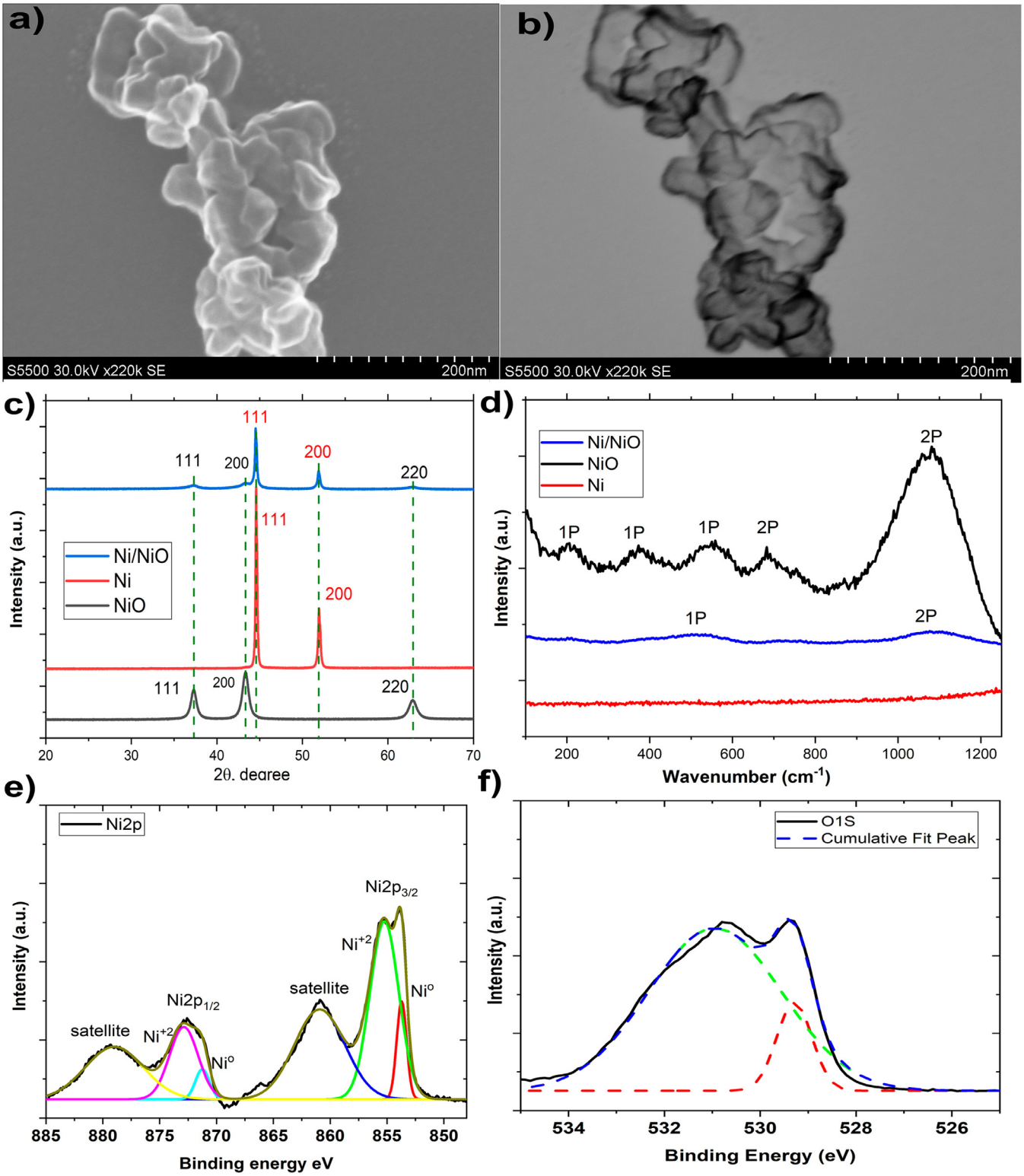

Fig. 2. a)and b) SEM images c) XRD patterns d) Raman spectrum of nickel catalysts (Ni, NiO, and Ni/NiO) synthesized by chemical reduction. e) High-resolution XPS spectrum of Ni 2p of Ni/NiO and f) high-resolution XPS spectrum of O-1S of Ni/NiO. (For interpretation of the references to colour in this figure legend, the reader is referred to the web version of this article.)

work of fused nanosheets [19,1,20]. The chemical reduction process has been reported to yield similar catalyst morphology such as nanocotton [21], nanosponges [22,23,24,25,26], and nanosheets [27,28,29,30,19,20]. In this work we will refer to the morphology in Fig. 2 as nanosheets.

The nanosheet morphology can be explained as being due to hydrogen evolution during catalyst synthesis. Hydrogen bubbles are being formed during chemical reduction, play a significant role in the creation of nanosheet morphology [31]. The hydrogen bubbles will produce strong disturbance on the structure and

particle size, making an amorphous phase and large surface area nanosheets [32]. The chemical reactions for catalyst formation with $NaBH_4$ can be described as follows (where M represent metals such as Ni): [31,33]

$$NaBH_{4(aq)}+2H_2O_{(\ell)} \rightarrow 4H_2\uparrow + NaBO_2 \quad (5)$$

$$4M(NO_3)_2+8NaBH_4+18H_2O \rightarrow 2M_2B\downarrow +8NaNO_3+25H_2\uparrow +6B(OH)_3 \quad (6)$$

Fig. 2c shows X-ray diffraction (XRD) patterns of Ni, NiO, and Ni/NiO catalysts. The NiO XRD pattern shows three distinct peaks at 37.2°, 43.2°, and 62.8° The NiO XRD peaks at 37.2°, 43.2°, and 62.8° correspond to (111), (200), and (220) diffraction planes of face-centered cubic (FCC) NiO (JCPDS card 47–1049) [34]. The high peak intensity indicates that NiO samples are of high crystallinity.

For Ni catalyst, the XRD pattern shows two diffraction peaks at 44.5° and 51.9°. The peaks at 44.5° and 51.9° correspond to Ni (111), and Ni (200) crystal planes of nickel FCC structure with JCPDS card 04–0850 [35]. The Ni/NiO catalyst shows peaks at 2θ values of 37.2°, 43.2°, and 62.8°, 44.5°, and 51.9° which correspond to the superposition of the diffraction patterns for Ni and NiO crystal structures.

Fig. 2d shows the Raman spectra for Ni, NiO, and Ni/NiO catalysts. Ni does not show any peaks in the Raman spectrum as Ni face-centered cubic (FCC) metal has a single atom primitive unit cell and does not show any polarizability change due to the interaction between the electric field of the monochromatic light and dipole moment within the material [13,36]. The NiO Raman spectrum shows peaks at 400, 530, 730, 900, 1090 cm^{-1} while the Ni/NiO Raman spectrum shows three peaks at 530 and 1090 cm^{-1}. The Raman peaks at 400 and 530 cm^{-1} correspond to one-phonon (1P) transverse optical (TO) and (1P) longitudinal optical (LO) of NiO vibrational modes, respectively [37,38]. The peaks at 730, 900, 1090 cm^{-1} correspond to two- phonon $2P_{TO}$, $2P_{TO+LO}$, and $2P_{LO}$ of NiO vibrational modes, respectively [37,38]. The existence of LO mode can be attributed to the disorder induced by defects and surface imperfectness [37,38].

X-ray photoelectron spectroscopy (XPS) was employed for further investigation of the surface chemistry and chemical states of Ni/NiO catalyst. The XPS survey spectrum contained peaks at 191.5 eV, 282 eV, 530.6 eV, and 855.5 eV that correspond to B, C, O, and Ni elements [39] (For the full spectrum, see in Figure S1). The Ni-2p high-resolution XPS spectrum is shown in Fig. 2e. The Ni-2p spectrum contains two main peaks Ni-$2p_{1/2}$ and Ni-$2p_{3/2}$ due to spin-orbit coupling [40]. Both Ni^0 and Ni^{2+} peaks clearly contribute to the spectra. The Ni-2p XPS spectrum shows two peaks at 853.8 eV, and 871.4 eV corresponds to Ni-$2p_{3/2}$ and Ni-$2p_{1/2}$ of metallic Ni, respectively. The XPS peak at 855.5 eV with a satellite at 860.9 eV corresponds to Ni-$2p_{3/2}$ of NiO. The XPS peak at 872.5 eV with a satellite at 879.4 eV corresponds to Ni-$2p_{1/2}$ of NiO [40]. A high-resolution XPS spectrum of the O 1S peak is shown in Fig. 2f. The O-1S XPS spectrum has been deconvoluted into two peaks at 529.35 and 531.7 eV. The peak at 529.35 eV can be assigned to metal-oxygen (Ni-O) bonds [41]. The peak at 531.7 eV can be attributed to surface species including hydroxides, absorbed oxygen, or absorbed water [41,42].

In summary, structural characterization shows that all nickel catalysts (Ni, NiO, and Ni/NiO) have the same nanosheet morphology. The XRD and ex-situ Raman spectroscopy indicate that catalyst with catalyst oxidation states equal to zero (in the Ni sample) and +2 (NiO sample), and both states in (Ni/NiO) sample were successfully produced. The XPS confirms the presence of both oxidation states in the Ni/NiO sample.

4. Electrochemical characterization

Fig. 3a shows linear sweep voltametry of nickel catalysts with different oxidation states in 1 M KOH. The Ni/NiO heterostructure has the lowest onset potential, −180 mV compared to −300 mV for bare Ni or NiO. We have taken the onset potential from Fig. 3a as the potential at which the absolute value of the current normalized to the geometric area has risen 5% above the double layer current.

With Ni/NiO a current density of −10 mA/cm^2 is obtained at a potential of −226 mV, as compared to Ni or NiO which require −354 mV and −372 mV, respectively, to reach the same current density in 1 M KOH. Fig. 3b presents Ni/NiO behavior in various electrolytes from DI water (18.2 MΩ.cm, Milli-Q water) to 1 M KOH. The HER activity of the Ni/NiO catalyst increases as the KOH concentration increase. Fig. 3c displays Tafel plots of nickel catalysts with different oxidation states. All catalysts have Tafel slopes in the same order of magnitude, that of the Ni/NiO heterostructure (135 mV/dec) being somewhat lower than the Tafel slopes of Ni (145 mV/dec) and NiO (165 mV/dec).

All nickel catalysts had the same BET surface area of 22±2 m^2/g (Figure S2), However, as inferred from the double layer capacitances the ESCA of the Ni/NiO was almost two times that of bare Ni or NiO. Normalizing HER activity electrochemical surface area (ECSA) shows that Ni/NiO possesses the superior HER activity (see Figure S2 in the Supporting Information) [5,8]. This shows that the superior activity of the Ni/NiO catalyst is an intrinsic increase and not trivially related to the surface area being larger.

During the HER at the Ni/NiO catalyst, the NiO phase has been suggested to promote the dissociation of the absorbed water by weakening O–H, and the H atom moves to Ni site for recombination to generate H_2 [9]. Bare NiO is poor at catalyzing the HER, owing to its inability to stabilize the H atom. At a bare Ni catalyst, the catalyst surface will be occupied by OH^- anion generated and thus blocking the active sites [9].

At higher KOH concentration the increase in the HER current density has been suggested to be due to the higher hydroxide ion activity, fast hydroxide ion migration rate, reaction kinetics, and diffusion rates [43,44,45]. Lasia et al. found that the rate constants k_i of Volmer and Heyrovsky reactions depend on OH concentration [43,44,45]. Recently wang et al. shows that the high Her activity at high KOH concentration is due to in-situ H_3O^+ intermediates generated on nanocatalyst surface [46].

The Tafel slope for the HER at Ni/NiO is close to 120 mV/dec, suggesting that the rate-determining step is the Volmer reaction in these alkaline electrolytes [45]. The HER reaction is frequently described in terms of two possible reaction pathways, the Volmer–Heyrovsky or the Volmer–Tafel mechanism, as illustrated in Fig. 3d. These mechanisms represent two different combinations of the Volmer, Heyrovsky, and Tafel reactions. The Volmer reaction involves the electroreduction of water molecules with hydrogen adsorption, while The Heyrovsky reaction involves electrochemical hydrogen desorption, and Tafel reaction involves chemical desorption as in eq (7), (8), and (9) below [45].

$$M + H_2O + e^- \rightleftharpoons MH_{ads} + OH^- \quad \text{Volmer} \quad (7)$$

$$MH_{ads} + H_2O + e^- \rightleftharpoons H_2 + M + OH^- \quad \text{Heyrovsky} \quad (8)$$

$$MH_{ads} + MH_{ads} \rightleftharpoons H_2 + M \quad \text{Tafel} \quad (9)$$

5. In-situ raman spectroscopy

Fig. 4 introduces cyclic voltammograms of Ni, NiO, and Ni/NiO catalysts and corresponding Raman spectrums at (0.2, 0.1, 0, −0.1, and −0.2 V vs RHE).

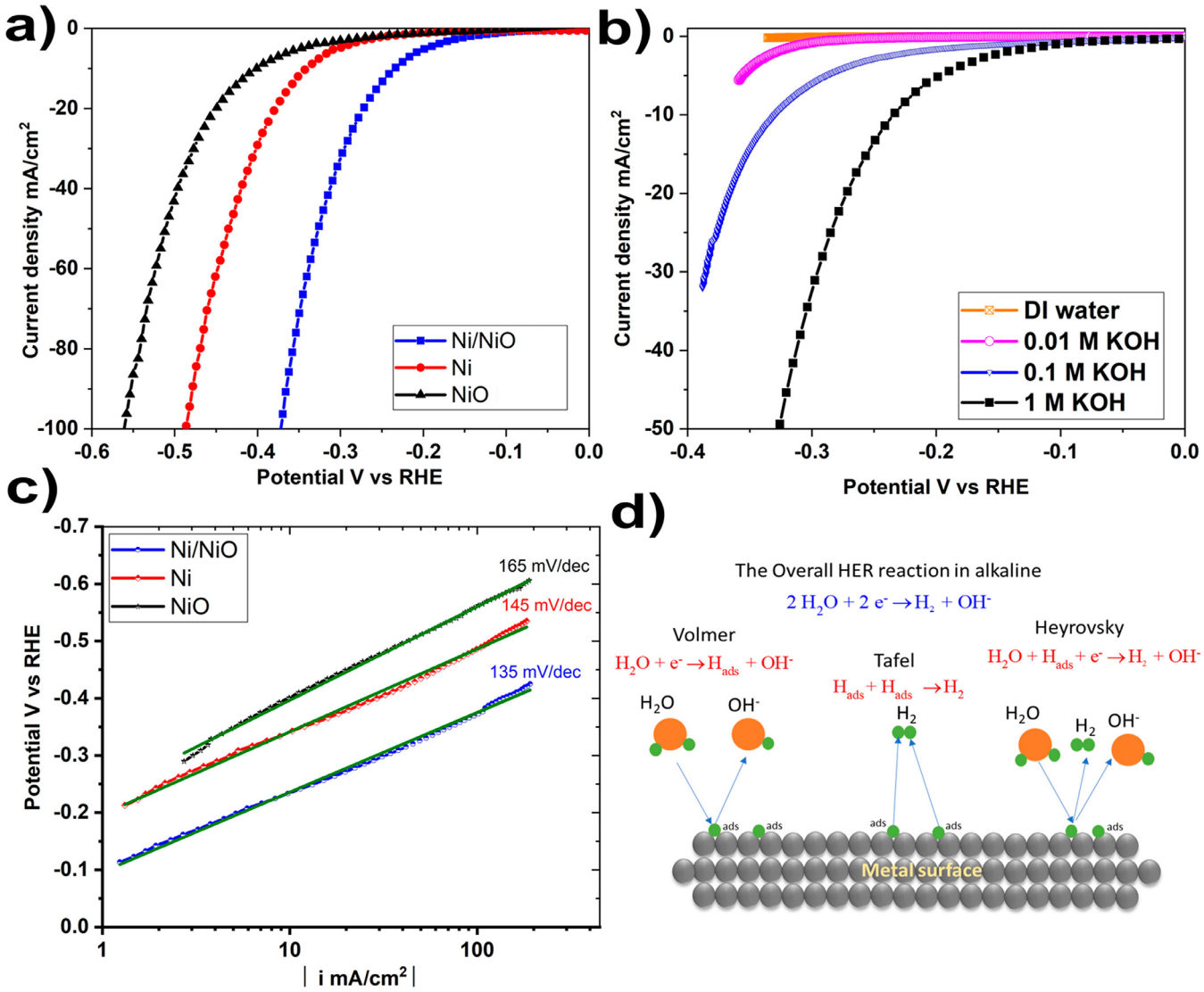

Fig. 3. a)HER polarization curves of various nickel catalysts in 1 M KOH, b) HER polarization curves of Ni/NiO catalyst obtained in various electrolytes, c) Tafel analysis of nickel catalysts in 1 M KOH, and d) Schematic of HER mechanism in alkaline electrolyte.

Ni nanosheets: Fig. 4a shows a cyclic voltammogram (CV) of Ni catalyst in 1 M KOH. The Ni CV exhibits typical features of Ni metal electrodes in alkaline media with an anodic peak and a cathodic peak attributed, respectively, to the formation and reduction of α-Ni(OH)$_2$.[8,17] When Ni metal is scanned in the positive direction, the Ni surface is converted to $\alpha-$Ni(OH)$_2$. The surface $\alpha-$Ni(OH)$_2$ will be reduced to Ni if scanned in the negative direction since $\alpha-$Ni(OH)$_2$ is easily reducible, provided the electrode potential does not exceed approximately 0.5 V at a scan rate higher than 20 mV/sec [17,18].

$$Ni + 2OH^- \rightarrow \alpha - Ni(OH)_2 + 2e^- \quad (10)$$

The Ni surface exposed to air oxidizes rapidly to a structure of 2–5 NiO layers terminated with OH. The OH termination will become Ni(OH)$_2$ Upon insertion into an alkaline solution. However, the air-formed oxide is reduced by applying HER potential on the electrode [47].

Fig. 4b shows the Raman spectrum of Ni catalyst in 1 M KOH at various applied potentials. The Raman spectrum at anodic potentials displays Raman peaks at 460 cm^{-1} and 1637 cm^{-1}, which correspond to α-Ni(OH)$_2$ and OH bending mode of H_2O respectively [42,48,49]. There is a clear potential dependence of the α-Ni(OH)$_2$ Raman mode. The surface α-Ni(OH)$_2$ Raman peak is only present at positive potentials and disappears once the HER starts. The in-situ Raman spectrum shows that an α-Ni(OH)$_2$ is present on the Ni nanosheet surface and that this α-Ni(OH)$_2$ gets reduced at negative potentials.

NiO nanosheets: Fig. 4c shows the CV of NiO in 1 M KOH. The NiO CV does not reveal any α-Ni(OH)$_2$ formation or reduction peaks. This is to be expected since the surface will be covered with a β-Ni(OH)$_2$ layer [18,50].

Raman spectra of NiO in 1 M KOH at various applied overpotentials are presented in Fig. 4d. The Raman spectra contain peaks at 446, 519, and 1637 cm^{-1}. The Raman peak at 1637 cm^{-1} corresponds to an OH bending mode of H_2O [42]. The Raman band at 446 cm^{-1} is related to metal-oxygen vibrations (ν Ni–O) A_{1g} in β-Ni(OH) $_2$. The Raman peak at 519 cm^{-1} is best assigned to a second-order acoustic mode of β-Ni(OH)$_2$ [51,52,53,54,55,42,56,52]. The potential dependence of the Raman spectra of surface β-Ni(OH)$_2$ on NiO is presented in Fig. 4d. The Raman mode corresponding to surface β-Ni(OH)$_2$ only appears when NiO is subjected to positive potentials (0 mV, 100 mV, and 200 mV in the Figure), while it vanishes once the HER starts.

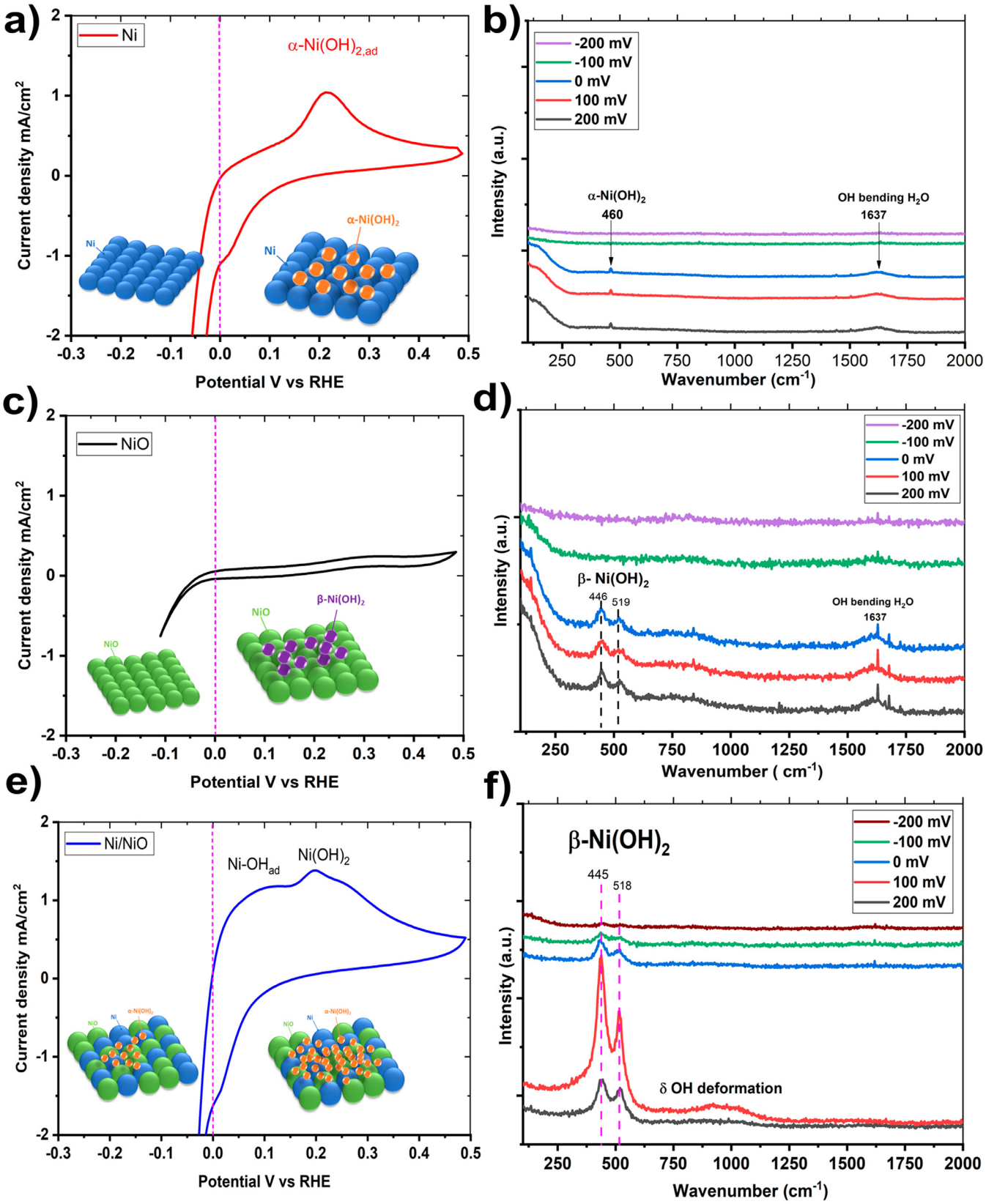

Fig. 4. Cyclic voltametry of a)Ni c) NiO and e) Ni/NiO nanosheets catalyst synthesized by chemical reduction in 1 M KOH. The corresponding in situ Raman spectra are shown in b) Ni d) NiO, and f) Ni/NiO at different applied overpotentials in 1 M KOH. (For interpretation of the references to colour in this figure legend, the reader is referred to the web version of this article.)

Ni/NiO nanosheets: Fig. 4e shows the CV of Ni/NiO catalyst in 1 M KOH. The Ni/NiO CV exhibits two anodic peaks for $Ni(OH)_{2,ad}$ and $Ni–OH_{ad}$, as compared to one single peak of $Ni(OH)_{2,\ ad}$ for bare Ni [8]. The second peak in the Ni/NiO CV appears at around $E \approx 0.10$ V [57,58,32,59,60,61,62,63]. The peak amplitude and position depend on the pretreatment of the electrode surface, measurement procedure and positive and negative potential limits of the CV [64,51]. Several processes have been proposed for the peak observed in Ni/NiO catalysts at a potential interval from 0.05 V through 0.15 V, such as adsorption of hydroxide-ions with the formation of $Ni–OH_{ad}$ [63], oxidation of adsorbed hydrogen [57,62], oxidation of absorbed hydrogen or Ni hydrides [57,58,32,60,61,63] and hydrogen desorption due to the presence of β-$Ni(OH)_2$ [65,60]. Fig. 4f shows the Raman spectrum of Ni/NiO in 1 M KOH. The Raman spectrum shows two peaks at 445 and 518 cm^{-1}. The band at 445 cm^{-1} can be attributed to metal-oxygen vibrations for the A_{1g} type stretch of Ni−O in β-$Ni(OH)_2$. The band at 518 cm^{-1} is assigned to a second-order acoustic mode of β-$Ni(OH)_2$ [52,55,42,56,52]. The Raman spectrum in Fig. 3f shows a clear broad peak at 980 cm^{-1} which can be assigned to OH deformation in water [66]. The Raman mode corresponding to surface β-$Ni(OH)_2$ is preserved when Ni/NiO is subjected to all potentials which is different than Ni or NiO behavior.

6. Short term durability

Fig. 5a shows the short term durability of Ni, NiO, and Ni/NiO catalysts for 10,000 sec at an applied potential of −0.4 V vs. RHE in 1 M KOH. Fig. 5a indicates that Ni/NiO gradually loses its initial activity and ends up at the same level as other nickel catalysts. Under −0.4 V vs. RHE applied potential, Ni/NiO activity deteriorates, NiO activity increases while Ni is stable.

Figs. 5b, 5c, and 5d display in situ Raman spectra of nickel catalysts (Ni, NiO, and Ni/NiO) under −0.4 V vs. RHE applied potential at various time intervals during the chronoamperometry experiment. The Raman modes of α-$Ni(OH)_2$ and β-$Ni(OH)_2$ disappear in the spectra recorded at 1000 sec for the Ni and NiO catalysts. For Ni/NiO the in-situ Raman spectra continue to display β-$Ni(OH)_2$ Raman modes at 1000 sec and disappears after that (2000 sec).

Fig. 5e shows the in-situ Raman spectrum of all catalysts (Ni, NiO, and Ni/NiO) after 10,000 sec. The Raman spectra for all nickel catalysts show a broad peak at 550–900 cm^{-1} range. This Raman feature can be assigned to a hydrated nickel that has been previously reported to exhibit features at 550–950 cm^{-1} with a more specific peak at 840 cm^{-1} [67,68,42]. The broad peak from 3100 to 3600 cm^{-1} is related to the O−H stretching of water [52,55]. These results show that regardless of the initial Ni catalyst oxidation state, by applying a large cathodic potential all catalysts behave like Ni after 10,000 sec.

At negative applied potentials, hydrogen absorption into Ni metal lattice with further formation of Ni hydrides proceed along with the reduction of Ni surface oxide species [47]. Hall et al. observed bulk α- or β-NiH by XRD for Ni electrodes held at currents more negative than −0.3 A/cm^2 [47]. The hydrogen incorporation into Ni electrode materials may take place by either permeation of hydrogen into Ni interstitial sites or by a transition to a nickel hydride phase [47,69].

Fig. 5f shows the ex-situ Raman spectrum of various nickel catalysts after chronoamperometry. All nickel catalysts, whatever the oxidation state, lead to nickel hydroxide surface coverage when the electrode reacts with ambient air after chronoamperometry. The Raman spectra show two distinct peaks at 450 and 530 cm^{-1}. The peak at 450 cm^{-1} is attributable to Ni−O bands in $Ni(OH)_2$ [52,55,42,56,52]. The band at 530 cm^{-1} are best assigned to defective or disordered $Ni(OH)_2$ [52,55,42,56,52]. Danilovic et al. showed, using XPS, that Ni metal exhibits oxide/hydroxide species after HER electrochemistry of the same features as $Ni/Ni(OH)_2$ [10].

7. Discussion

The most important finding in this work is the direct demonstration through Raman spectroscopy of the slow convergence of the surface states of the NiO and Ni/NiO catalysts toward that of Ni (Fig. 5). The initial catalytic activity correlates directly with the surface states as evidenced by the Raman spectra. These results show that the mixed oxidation state of Ni/NiO has a superior catalytic activity as compared to the more homogenous catalyst Ni and NiO, in line with findings of Pan, Oshchepkov, Dong et.al [70,71,72]. However, as the Ni/NiO catalyst is exposed to the high negative electrode potentials associated with the HER the surface state slowly changes to the Ni, as evidenced by the broad featureless Raman spectrum in Fig. 5d for 4000 sec. For the NiO catalyst, the result is the opposite, and the catalyst becomes more active as it is being reduced along with its surface state changing to that of Ni. The catalysts thus end up with the same surface and the same catalytic activity due to the load potentials of the hydrogen evolution reaction. These results, therefore, show that although the observation that a mixture of oxidation states gives a high catalytic activity, the catalysts cannot be expected to maintain such a mixture of oxidation more than a short period at the low potentials associated with the hydrogen evolution reaction. The design of a stable catalyst should, therefore, include means of stabilizing both oxidation states in nickel.

The effect of the oxidation state here is intrinsic and not related to differences or changes in the surface area. The BET surface area of various nickel catalysts was not changed while the electrochemical surface area of Ni/NiO nanosheets was two times that of Ni or NiO nanosheets which indicates the higher availability of active sites in Ni/NiO. Normalizing HER current to the ECSA, Ni/NiO still displays superior HER activity (Figure S2) so the higher intrinsic activity is not only due to surface area enhancement [10]. Another interesting fact brought out by the Raman spectra is that the beta nickel hydroxide β-$Ni(OH)_2$ is capable of catalyzing the HER to a similar degree as other oxides or hydroxides. The similarity of the Tafel slopes for the catalysts indicates that the *rds* are the same for all the catalysts, and the fact that the values are close to 120 mV suggests that the Volmer step is rate-determining. Due to the presence of both Ni, and NiO/β-$Ni(OH)_2$ at the same surface facilitates water dissociation resulting in OH_{ad} at the NiO/β-$Ni(OH)_2$ and H_{ads} at metallic (elemental) Ni [10].

Similar work by Oshchepkov et al. showed that Ni/NiO_x attained by electrochemical oxidation has a maximum HER activity at 30% NiO_x coverage [72]. A kinetic model proposed that the HOR/HER activity due to the dependence of H_{ad} strength on NiO_x coverage that elevates the Volmer reaction rate. Lovell et al. showed that Ni/NiO combination enabled by the oxidative pretreatment, provides an optimized density of both NiO and Ni and facilitate both the adsorption of H (Ni sites) and provide adsorption/desorption sites for OH species (NiO sites) [73]. Danilovic et al. [10]. showed that $Ni(OH)_2$/Ni surfaces prepared by chemical deposition are 3–5 fold more active than Ni bare substrate and that introduction of $Ni(OH)_2$ to Ni led to Tafel slopes approach 120 mV/dec suggesting the Volmer step as the rate-determining step [10]. Therefore, the type of oxide or hydroxide at the surface appears to be less important than the mere presence of such an oxide or hydroxide.

The Raman-potential dependence in Ni/NiO nanosheets showed a distinct behavior than Ni or NiO nanosheets. In situ Raman measurements shows that maintaining the surface β-$Ni(OH)_2$ initially present during HER is correlated with the HER activity of Ni/NiO nanosheets compared to Ni or NiO. NiO and Ni/NiO show the same

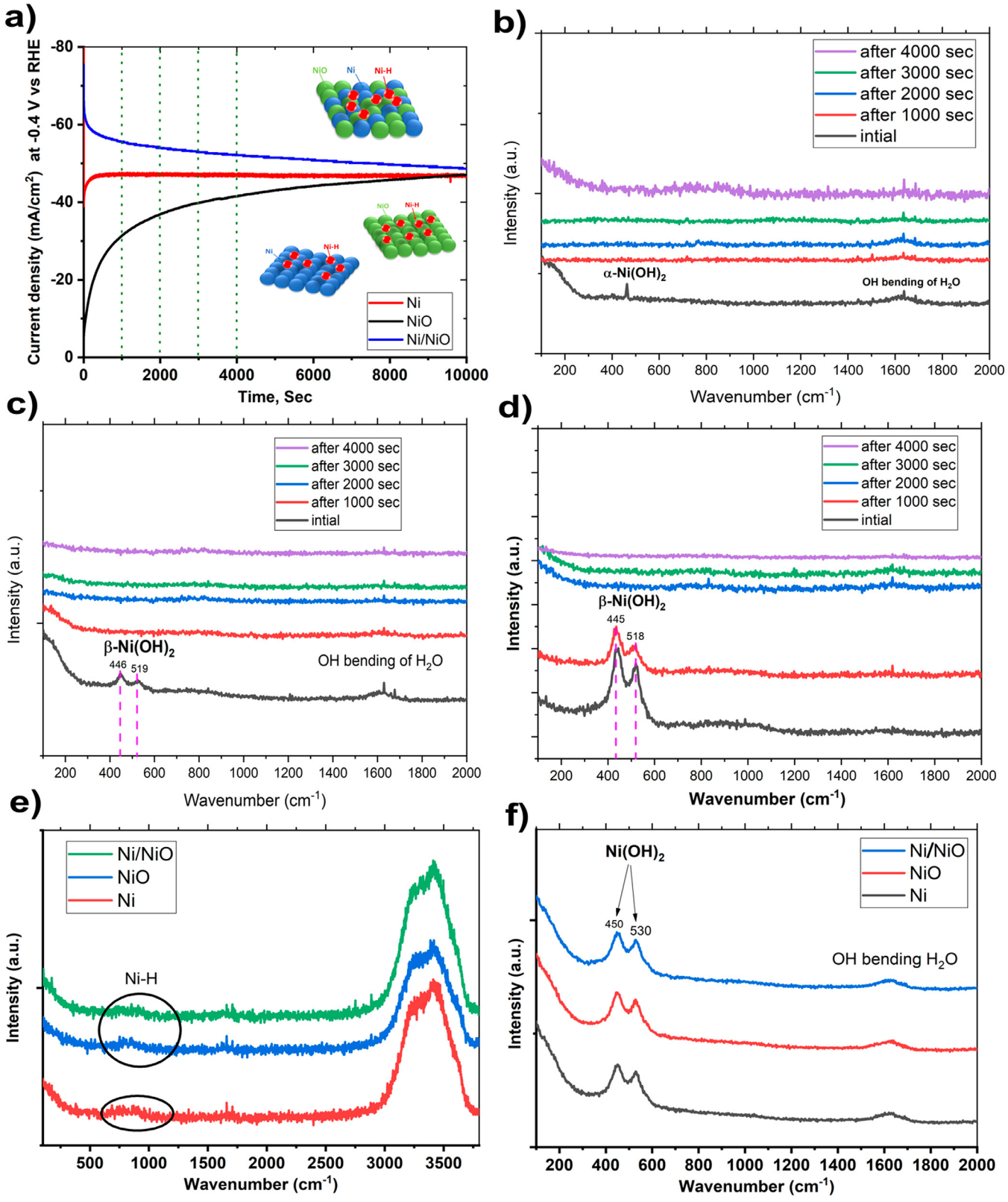

Fig. 5. a) Chronamperometry of Ni, NiO, and Ni/NiO nanosheets catalysts at −0.4 V vs RHE in 1 M KOH, in-situ Raman–chronoamperometry at different time intervals for b) Ni, c) NiO, and d) Ni/NiO. e) In-situ Raman after 10,000 sec and f) Ex-situ Raman spectrum of different Ni catalysts upon removal from the cell and exposure to the ambient atmosphere after the chronoamperometry test.

β-Ni(OH)$_2$ species, however, only Ni/NiO shows higher HER activity and maintained initially the hydroxide species which confirmed the importance of Ni metal sites in addition to oxide sites for maintaining nickel hydroxide species and the superior HER activity. Danilovic et al. [10]. showed that NiO thermal oxide exhibits low HER activity compared to Ni metal surface confirming the importance of metal sites for the HER. Danilovic et al. [10]. showed also that the addition of Ni(OH)$_2$ to NiO led to no enhancements in HER activity for NiO demonstrating the importance of Ni metal sites for the H recombination reaction and oxide site to dissociate water and increasing the overall rates of HER [10].

Although Tafel slopes indicate a mechanism that does not involve a hydroxide layer at all, the formation of the hydroxide layer on NiO is likely to happen after cycling or during handling in alkaline electrolytes. When NiO is cycled in $0 \leq E \leq 0.5$, the surface is probably covered with β-Ni(OH)$_2$ [18,50]. while in the case of Ni in the same potential range, the surface is covered with a few monolayers of easily reducible α-Ni(OH)$_2$ [8,17]. Bates et al. reported the presence of a higher degree of oxides like Ni(OH)$_2$ in Ni/NiO by X-ray absorption spectroscopy (XAS) analysis [11]. In the presence of humid air, NiO will form Ni(OH)$_2$ top layer that will be thickened with immersion in the alkaline solution [74,75,8].

The presence of metal and oxide species is crucial to maintain β-Ni(OH)$_2$ species initially which explain why Ni/NiO had higher HER activity compared to NiO that initially showed the same β-Ni(OH)$_2$ or Ni that showed the presence of the easily reducible α-Ni(OH)$_2$. β-Ni(OH)$_2$ is harder to reduce than α-Ni(OH)$_2$ [58,60]. However Hall et al. proposed the possibility of β-Ni(OH)$_2$ at higher negative potentials [47] however, Under the application of a high negative potential (−0.4 V vs RHE) for 2000 sec, the reduction of β-Ni(OH)$_2$ on Ni/NiO nanosheets occurs and the HER activity deteriorated. The loss of β-Ni(OH)$_2$ species on Ni/NiO nanosheets causes the performance deterioration of Ni/NiO nanosheets as in Fig. 5a. which agree with the literature [76]. Hall et al. reported that β-Ni(OH)$_2$ may be reduced to Ni on the HER potential range [47]. NiO nanosheets HER activity improves by time as part of NiO species gets reduced to Ni under prolonged HER (under the applied potential of (−0.4 V vs RHE). The presence of in situ generated Ni^0 species increases NiO HER activity. The improved NiO activity under prolonged HER negative potential confirms also that the presence of in-situ reduced Ni and non-reduced NiO improves HER activity. Similar reports by wang et al. showed that bulk Ni^0 and in-situ formed Ni$^\circ$ from NiO will facilitate water splitting and improve HER activity of NiO [77].

In summary, the results here agree with previous reports that Ni/NiO loses its high initial activity after applying cathodic potential for a considerable duration [11,4]. Regardless of the initial nickel nanosheets oxidation state, after applying high cathodic potential, all catalysts behaved like Ni after 10,000 sec. The findings also confirmed the importance of Ni metal sites in addition to oxide sites and maintaining hydroxide species for superior and durable HER activity. Blending Ni/NiO nanosheets with another metal oxide such as Cr_2O_3 or Fe_3O_4 [11,4,78] or directly deposit stable Ni(OH)$_2$ [10] can be the solution to preserve the superior HER activity of Ni/NiO nanosheets.

8. Conclusions

Various nickel catalysts with different oxidation states (Ni, NiO, and Ni/NiO nanosheets) were synthesized by chemical reduction using sodium borohydride. Ni/NiO nanosheets catalyst exhibited superior alkaline HER activity compared to Ni or NiO bare. A Tafel analysis indicated that the Volmer step is the rate-determining step. The HER process of Ni/NiO was found to be dependent on the OH^- concentration, increasing with increasing KOH concentration in the concentration range investigated (0.01 to 1 M KOH). In situ Raman spectro-electrochemistry showed that Ni/NiO nanosheet heterostructures initially maintained the β-Ni(OH)$_2$ during HER. However, this β-Ni(OH)$_2$ layer gradually disappeared in the Ni/NiO nanosheets lost if the electrode was maintained at −0.4 V vs. RHE for more than 2000 sec. Regardless of the initial oxidation state of the nickel, under the applications of large and negative potentials, all catalysts behaved like Ni after 10,000 sec. The results emphasize the importance of both Ni metal sites and oxide sites being present in the same catalyst and maintaining hydroxide species for a superior and durable HER activity.

Declaration of Competing Interest

There are no conflicts to declare.

Acknowledgments

This work was performed within HAPEEL project “Hydrogen Production by Alkaline Polymer Electrolyte Electrolysis” financially supported by the Research Council of Norway-ENERGIX program contract number 268019 and the INTPART project 261620. The Research Council of Norway is acknowledged for the support to the Norwegian Micro- and Nano-Fabrication Facility, NorFab, project number 245963/F50.

Supplementary materials

Supplementary material associated with this article can be found, in the online version, at doi:10.1016/j.electacta.2020.137040.

References

[1] A. Faid, A. Oyarce Barnett, F. Seland, S. Sunde, A.Y. Faid, A. Oyarce Barnett, F. Seland, S. Sunde, Catalysts 8 (2018) 614.
[2] A.Y. Faid, A.O. Barnett, F. Seland, S. Sunde, J. Electrochem. Soc. 166 (2019) F519–F533.
[3] J.R. Varcoe, P. Atanassov, D.R. Dekel, A.M. Herring, M.A. Hickner, P.A. Kohl, A.R. Kucernak, W.E. Mustain, K. Nijmeijer, K. Scott, T. Xu, L. Zhuang, Energy Environ. Sci. 7 (2014) 3135–3191.
[4] M. Gong, W. Zhou, M.C. Tsai, J. Zhou, M. Guan, M.C. Lin, B. Zhang, Y. Hu, D.Y. Wang, J. Yang, S.J. Pennycook, B.J. Hwang, H. Dai, Nat. Commun. 5 (2014) 4695.
[5] D. Strmcnik, M. Uchimura, C. Wang, R. Subbaraman, N. Danilovic, D. Van Der Vliet, A.P. Paulikas, V.R. Stamenkovic, N.M. Markovic, Nat. Chem. 5 (2013) 300–306.
[6] J. Wang, S. Mao, Z. Liu, Z. Wei, H. Wang, Y. Chen, Y. Wang, ACS Appl. Mater. Interfaces 9 (2017) 7139–7147.
[7] Y. Dong, J. Dang, W. Wang, S. Yin, Y. Wang, ACS Appl. Mater. Interfaces 10 (2018) 39624–39630.
[8] A.G. Oshchepkov, A. Bonnefont, V.A. Saveleva, V. Papaefthimiou, S. Zafeiratos, S.N. Pronkin, V.N. Parmon, E.R. Savinova, Top. Catal. 59 (2016) 1319–1331.
[9] M. Gong, D.Y. Wang, C.C. Chen, B.J. Hwang, H. Dai, Nano Res 9 (2016) 28–46.
[10] N. Danilovic, R. Subbaraman, D. Strmcnik, K.-C. Chang, A.P. Paulikas, V.R. Stamenkovic, N.M. Markovic, Angew. Chemie 124 (2012) 12663–12666.
[11] M.K. Bates, Q. Jia, N. Ramaswamy, R.J. Allen, S. Mukerjee, J. Phys. Chem. C 119 (2015) 5467–5477.
[12] Y. Deng, B.S. Yeo, ACS Catal (7) (2017) 7873–7889.
[13] I.R. Lewis, H.G.M. Edwards, Handbook of Raman spectroscopy : from the research laboratory to the process line, Marcel Dekker, 2001.
[14] L. Trotochaud, S.L. Young, J.K. Ranney, S.W. Boettcher, J. Am. Chem. Soc. 136 (2014) 6744–6753.
[15] C.C.L. McCrory, S. Jung, I.M. Ferrer, S.M. Chatman, J.C. Peters, T.F. Jaramillo, J. Am. Chem. Soc. 137 (2015) 4347–4357.
[16] M. Alsabet, M. Grden, G. Jerkiewicz, Electrocatalysis 5 (2014) 136–147.
[17] M. Alsabet, M. Grden, G. Jerkiewicz, Electrocatalysis 2 (2011) 317–330.
[18] M. Grdeń Michałand Alsabet, G. Jerkiewicz, M. Grdeń, M. Alsabet, G. Jerkiewicz, M. Grdeń Michałand Alsabet, G. Jerkiewicz, M. Grdeń, M. Alsabet, G. Jerkiewicz, ACS Appl. Mater. Interfaces 4 (2012) 3012–3021.
[19] J.M.V. Nsanzimana, V. Reddu, Y. Peng, Z. Huang, C. Wang, X. Wang, Chem. - A Eur. J. 24 (2018) 18502–18511.
[20] T. He, J. Marie, V. Nsanzimana, R. Qi, J.Y. Zhang, M. Miao, Y. Yan, K. Qi, H. Liu, B.Y. Xia, J.M.V. Nsanzimana, R. Qi, J.Y. Zhang, M. Miao, Y. Yan, K. Qi, H. Liu, B.Y. Xia, J. Mater. Chem. A 6 (2018) 23289–23294.
[21] S. Wang, P. He, Z. Xie, L. Jia, M. He, X. Zhang, F. Dong, H. Liu, Y. Zhang, C. Li, Electrochim. Acta 296 (2019) 644–652.

[22] C. Zhu, D. Wen, S. Leubner, M. Oschatz, W. Liu, M. Holzschuh, F. Simon, S. Kaskel, A. Eychmüller, Chem. Commun. 51 (2015) 7851–7854.
[23] K.S. Krishna, C.S.S. Sandeep, R. Philip, M. Eswaramoorthy, S. Fu, J. Song, C. Zhu, G.L. Xu, K. Amine, C. Sun, X. Li, M.H. Engelhard, D. Du, Y. Lin, Q. Lu, J. Huang, C. Han, L. Sun, X. Yang, K.S. Krishna, C.S.S. Sandeep, R. Philip, M. Eswaramoorthy, N.A. Nguyen, H.S. Choi, Y. Wang, H. Chen, S. Dong, E. Wang, ACS Nano 4 (2010) 2681–2688.
[24] S. Fu, C. Zhu, J. Song, M.H. Engelhard, Y. He, D. Du, C. Wang, Y. Lin, J. Mater. Chem. A 4 (2016) 8755–8761.
[25] Q. Lu, J. Huang, C. Han, L. Sun, X. Yang, Electrochim. Acta 266 (2018) 305–311.
[26] N.A. Nguyen, V.T. Nguyen, S. Shin, H.S. Choi, J. Alloys Compd. 789 (2019) 163–173.
[27] Y. Jiang, Y. Fang, C. Chen, P. Ni, B. Kong, Z. Song, Y. Lu, L. Niu, ChemElectroChem 6 (2019) 3684–3689.
[28] J. Masa, I. Sinev, H. Mistry, E. Ventosa, M. de la Mata, J. Arbiol, M. Muhler, B. Roldan Cuenya, W. Schuhmann, Adv. Energy Mater. 7 (2017) 1700381.
[29] X. Chen, Z. Yu, L. Wei, Z. Zhou, S. Zhai, J. Chen, Y. Wang, Q. Huang, H. Enis Karahan, X. Liao, Y. Chen, J. Mater. Chem. A 7 (2019) 764–774.
[30] H. Sun, X. Xu, Z. Yan, X. Chen, L. Jiao, F. Cheng, J. Chen, J. Mater. Chem. A 6 (2018) 22062–22069.
[31] J. Marie, V. Nsanzimana, R. Dangol, V. Reddu, S. Duo, Y. Peng, K.N. Dinh, Z. Huang, Q. Yan, X. Wang, ACS Appl. Mater. Interfaces 11 (2018) 846–855.
[32] Y. Yang, L. Zhuang, T.E. Rufford, S. Wang, Z. Zhu, RSC Adv 7 (2017) 32923–32930.
[33] S. Gupta, M.K. Patel, A. Miotello, N. Patel, Adv. Funct. Mater. 30 (2020) 1906481.
[34] H. Yan, D. Zhang, J. Xu, Y. Lu, Y. Liu, K. Qiu, Y. Zhang, Y. Luo, Nanoscale Res. Lett. 9 (2014) 1–7.
[35] R. Ding, J. Liu, J. Jiang, F. Wu, J. Zhu, X. Huang, Catal. Sci. Technol. 1 (2011) 1406.
[36] J.T.H. Kwan, A. Bonakdarpour, G. Afonso, D.P. Wilkinson, Electrochim. Acta 258 (2017) 208–219.
[37] N. Mironova-Ulmane, A. Kuzmin, I. Steins, J. Grabis, I. Sildos, M. Pärs, J. Phys. Conf. Ser. 93 (2007) 012039.
[38] G. George, S. Anandhan, RSC Adv 4 (2014) 62009–62020.
[39] J.M.V. Nsanzimana, L. Gong, R. Dangol, V. Reddu, V. Jose, B.Y. Xia, Q. Yan, J.M. Lee, X. Wang, Adv. Energy Mater. 9 (2019) 1901503.
[40] M. Chu, L. Wang, X. Li, M. Hou, N. Li, Y. Dong, X. Li, Z. Xie, Y. Lin, W. Cai, C. Zhang, Electrochim. Acta 264 (2018) 284–291.
[41] J. Yu, Y. Ni, M. Zhai, J. Phys. Chem. Solids 112 (2018) 119–126.
[42] Z. Qiu, C.W. Tai, G.A. Niklasson, T. Edvinsson, Energy Environ. Sci. 12 (2019) 572–581.
[43] H. Dong, T. Lei, Y. He, N. Xu, B. Huang, C.T. Liu, Int. J. Hydrogen Energy 36 (2011) 12112–12120.
[44] T. Zhang, X. Liu, X. Cui, M. Chen, S. Liu, B. Geng, Adv. Mater. Interfaces 5 (2018) 1800359.
[45] A. Lasia, Int. J. Hydrogen Energy 44 (2019) 19484–19518.
[46] X. Wang, C. Xu, M. Jaroniec, Y. Zheng, S.Z. Qiao, Nat. Commun. 10 (2019) 4876.
[47] D.S. Hall, C. Bock, B.R. MacDougall, J. Electrochem. Soc. 160 (2013) F235–F243.
[48] D.S. Hall, D.J. Lockwood, S. Poirier, C. Bock, B.R. MacDougall, J. Phys. Chem. A 116 (2012) 6771–6784.
[49] R. Kostecki, J. Electrochem. Soc. 144 (1997) 485.
[50] J. Van Drunen, B. Kinkead, M.C.P. Wang, E. Sourty, B.D. Gates, G. Jerkiewicz, ACS Appl. Mater. Interfaces 5 (2013) 6712–6722.
[51] N.A. Shumilova, V.S. Bagotzky, Electrochim. Acta 13 (1968) 285–293.
[52] M.W. Louie, A.T. Bell, J. Am. Chem. Soc. 135 (2013) 12329–12337.
[53] D.S. Hall, D.J. Lockwood, S. Poirier, C. Bock, B.R. MacDougall, ACS Appl. Mater. Interfaces 6 (2014) 3141–3149.
[54] D.S. Hall, D.J. Lockwood, C. Bock, B.R. MacDougall, Proc. R. Soc. A Math. Phys. Eng. Sci. 471 (2014) 20140792.
[55] X. Yu, J. Zhao, L.-.R. Zheng, Y. Tong, M. Zhang, G. Xu, C. Li, J. Ma, G. Shi, ACS Energy Lett (2018) 237–244.
[56] B.S. Yeo, A.T. Bell, J. Phys. Chem. C 116 (2012) 8394–8400.
[57] J.L. Weininger, M.W. Breiter, J. Electrochem. Soc. 111 (1964) 707.
[58] S.A. Machado, L.A. Avaca, Electrochim. Acta 39 (1994) 1385–1391.
[59] W. Visscher, E. Barendrecht, Surf. Sci. 135 (1983) 436–452.
[60] W. Visscher, E. Barendrecht, J. Appl. Electrochem. 10 (1980) 269–274.
[61] W. Visscher, E. Barendrecht, Electrochim. Acta 25 (1980) 651–655.
[62] A.G. Pshenichnikov, Mater. Chem. Phys. 22 (1989) 121–148.
[63] D. Floner, C. Lamy, J.M. Leger, Surf. Sci. 234 (1990) 87–97.
[64] L.D. Burke, T.A.M. Twomey, J. Electroanal. Chem. Interfacial Electrochem. 162 (1984) 101–119.
[65] A. Seyeux, V. Maurice, L.H. Klein, P. Marcus, J. Solid State Electrochem. 9 (2005) 337–346.
[66] R.L. Frost, K.H. Bakon, S.J. Palmer, J. Raman Spectrosc. 41 (2010) 78–83.
[67] W. Krasser, A.J. Renouprez, J. Raman Spectrosc. 8 (1979) 92–94.
[68] J.M. Nicol, Spectrochim. Acta Part A Mol. Spectrosc. 48 (1992) 313–327.
[69] N. Mironova-Ulmane, A. Kuzmin, I. Steins, J. Grabis, I. Sildos and M. Pärs, J. Phys. Conf. Ser., 2007, 93, 012039, DOI:10.1088/1742-6596/93/1/012039.
[70] Y. Dong, J. Dang, W. Wang, S. Yin, Y. Wang, ACS Appl. Mater. Interfaces 10 (2018) 39624–39630.
[71] Y. Pan, G. Hu, J. Lu, L. Xiao, L. Zhuang, J. Energy Chem. 29 (2019) 111–115.
[72] A.G. Oshchepkov, A. Bonnefont, E.R. Savinova, Electrocatalysis 11 (2020) 133–142.
[73] E.C. Lovell, X. Lu, Q. Zhang, J. Scott, R. Amal, Chem. Commun. 56 (2020) 1709–1712.
[74] S.L. Medway, C.A. Lucas, A. Kowal, R.J. Nichols, D. Johnson, J. Electroanal. Chem. 587 (2006) 172–181.
[75] E.S. Lambers, C.N. Dykstal, J.M. Seo, J.E. Rowe, P.H. Holloway, Oxid. Met. 45 (1996) 301–321.
[76] A.R.T. Morrison, L. Juillac, S. Guyomart, R. Wüthrich, J. Electrochem. Soc. 163 (2016) F3146–F3152.
[77] J. Wang, S. Mao, Z. Liu, Z. Wei, H. Wang, Y. Chen, Y. Wang, ACS Appl. Mater. Interfaces 9 (2017) 7139–7147.
[78] Y. Xie, X. Wang, K. Tang, Q. Li, C. Yan, Electrochim. Acta 264 (2018) 225–232.